

Measuring the magnon-photon coupling in shaped ferromagnets: tuning of the resonance frequency

Sergio Martínez-Losa del Rincón,^{1,2} Ignacio Gimeno,^{1,2} Jorge Pérez-Bailón,^{1,2} Victor Rollano,^{1,2} Fernando Luis,^{1,2} David Zueco,^{1,2} and María José Martínez-Pérez^{1,2,*}

¹*Instituto de Nanociencia y Materiales de Aragón (INMA), CSIC-Universidad de Zaragoza, Zaragoza, Spain*

²*Departamento de Física de la Materia Condensada, Universidad de Zaragoza*

Cavity photons and ferromagnetic spins excitations can exchange information coherently in hybrid architectures, at speeds set by their mutual coupling strength. Speed enhancement is usually achieved by optimizing the geometry of the electromagnetic cavity. Here we show that the geometry of the ferromagnet plays also an important role, by setting the fundamental frequency of the magnonic resonator. Using focused ion beam patterning, we vary the aspect ratio of different Permalloy samples reaching operation frequencies above 10 GHz while working at low external magnetic fields. Additionally, we perform broad band ferromagnetic resonance measurements and cavity experiments that demonstrate that the magnon-photon coupling strength can be estimated using either open transmission lines or resonant cavities, yielding very good agreement. Finally, we describe a simple theoretical framework based on electromagnetic and micromagnetic simulations that successfully accounts for the experimental results. This approach can be used to design hybrid quantum systems exploiting whatever magnetostatic mode excited in ferromagnets of arbitrary size and shape and to tune their operation conditions.

I. INTRODUCTION

In recent years, quantum manipulation and read-out protocols based on circuit quantum electrodynamics [1] have been successfully applied to the field of quantum magnonics [2–4]. In these studies, a coherent coupling between photons in an electromagnetic cavity and magnons in a ferromagnet is achieved in the strong [5, 6] and, even, ultra-strong regime [7, 8]. This has opened the way to the observation of interesting phenomena with strong potential for applications like quantum transduction between optical and microwave photons [9, 10], dispersive coupling between quantum systems [11–13] or non-reciprocal transmission of rf signals [14–17].

Electromagnetic cavities and ferromagnets are different versions of an harmonic oscillator, whose bosonic quanta of excitations correspond to photons and magnons, respectively. The resonant frequency of such cavities can be tuned by different means. This is relatively easy in the case of photons. For instance, size determines the fundamental modes in three dimensional microwave cavities and superconducting coplanar waveguide (CPW) resonators [18]. Superconducting thin-films are also used for the implementation of lumped element LC -resonators with fundamental frequencies given by $\omega_p = 1/\sqrt{LC}$, which is, in essence, a geometrical factor as well [18]. In the case of magnons, spins precess around the local effective magnetic field. This field results from the contribution of the externally applied magnetic field B_{ext} and the (much more difficult to calculate) demagnetizing field [19]. Again, the latter is determined by the geometry of the sample. In isotropic magnets, e.g. spheres, shape effects cancel out and the resulting reso-

nance frequency depends linearly on the external magnetic field as $\omega_m = \gamma_e B_{\text{ext}}$ [20] with $\gamma_e/2\pi = 28 \text{ GHz/T}$ the electron gyromagnetic ratio.

In most experiments performed so far, yttrium iron garnet (YIG) spheres strongly coupled to either three dimensional cavities [5, 8] or superconducting CPW resonators [11] have been the preferred choice. These magnets are commercial and exhibit record low Gilbert damping constant ($\alpha \sim 10^{-5}$), which is beneficial for the observation of long lived coherent exchange of information between the photonic and magnonic excitations. However, YIG spheres do not couple optimally to thin film superconducting circuits that are pivotal in quantum applications [1, 6]. YIG thin films are neither well suited for conventional lithography processes nor for cryogenic operation as the optimum substrate material for YIG growth becomes lossy with decreasing temperature [21]. For these reasons, other C-MOS compatible materials like Permalloy (Py, with a moderate $\alpha \sim 10^{-2}$) [7, 22, 23] or iron-cobalt alloys ($\text{Fe}_{75}\text{Co}_{25}$, with a very promising $\alpha \sim 10^{-3}$) are drawing attention [24, 25].

Yet, custom tuning of the resonance frequency of such magnetic cavities is still to be demonstrated. This is relevant since experimental conditions usually impose certain constraints due to the use of, e.g., circulators or amplifiers with narrow frequency bandwidth. Additionally, operating devices at high frequencies is interesting since the coupling strength g between photons and magnons increases linearly with the frequency. The reason is that g is given by the Zeeman coupling between the magnon dipole moment and the oscillating vacuum field in the cavity. The latter is:

$$b_{\text{rms}} = \sqrt{\frac{\mu_0 \hbar \omega_p}{2V_{\text{eff}}}}, \quad (1)$$

where, the sub-index denotes the root mean square (r.m.s.) and V_{eff} is the effective volume of the electro-

* pemar@unizar.es

magnetic mode. V_{eff} depends on the size of the electromagnetic wavelength (thus on the inverse frequency) yielding $g \propto \omega_p$.

Increasing g is usually accomplished by a geometrical optimization of the resonator, i.e., patterning of nanoconstrictions [26–28] and/or reducing the impedance of lumped LC -resonators which is equivalent to reducing V_{eff} [29, 30]. These approaches serve to confine b_{rms} within the (typically) small volume of the ferromagnet, yielding a square-root increase of the coupling. A larger (linear) enhancement of g should be achieved by working with high frequency superconducting resonators. However, the experimental observation of such high frequency effect in isotropic ferromagnets requires polarizing the magnetization with strong magnetic fields that are detrimental for the operation of superconducting circuits.

Here we show a direct way to tune the resonance frequency of suitably shaped micron-sized Py samples while keeping the external magnetic field below few tens of mT. Using superconducting CPW transmission lines we first show that, depending on the aspect ratio of the ferromagnet, the broadband ferromagnetic resonance (FMR) spectra can be modified at will. We then convert the transmission lines into cavities by opening gap capacitors. We demonstrate that both approaches can be used to experimentally estimate the coupling factors. Our experiments are complemented with a general-purpose theoretical model including realistic electromagnetic and micromagnetic simulations.

II. RESULTS

A. Sample fabrication

We use four CPW superconducting transmission lines fabricated by optical lithography on 150 nm thick Niobium films deposited by sputtering onto single crystalline sapphire substrates (see Fig. 1a top). A constriction of width w is opened in the central part of two transmission lines by focused ion beam (FIB) milling using moderate currents which result in lateral resolutions below 10 nm (see Fig. 1a bottom). These constrictions, with dimensions matching those of the different samples, serve to locally focus b_{rms} , yielding enhanced coupling with the smallest ferromagnets.

On the other hand, Py thin-films of various thicknesses t are e-beam evaporated onto 500 nm-thick Si_3N_4 membranes. The ferromagnets are patterned by FIB milling to produce four different samples labelled #1 to #4 whose dimensions are summarized in Fig. 2a. Finally, an Omniprobe needle inside the FIB microscope is used to transport a micrometric sized Si_3N_4 palette containing the Py sample to precise positions on top of the superconducting circuit reaching optimum coupling. For this purpose, it is important to minimize the distance h between the ferromagnet and the superconducting line (Fig. 1b). This is difficult in case of sample #2 due to its large

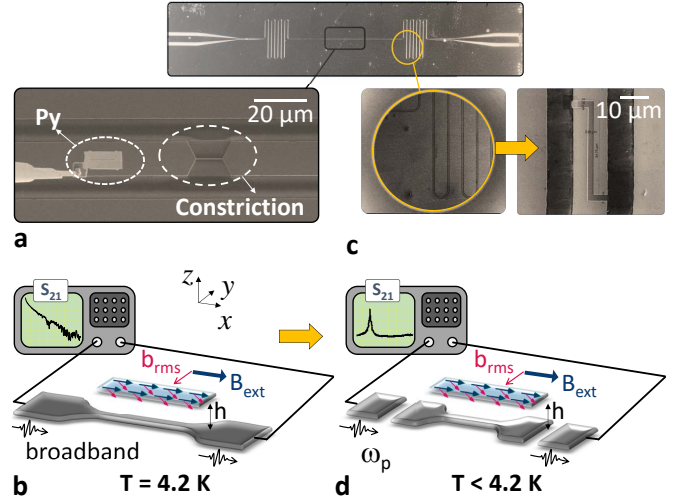


FIG. 1. **a**: A constriction of width w is FIB patterned on the central part of a conventional Nb CPW transmission line. The Omniprobe needle is used to transport the Si_3N_4 palette with the Py ferromagnet towards the constriction. **b**: Broadband FMR experiments are performed by measuring the S_{21} transmission parameter with a VNA while sweeping the external magnetic field B_{ext} applied along the \hat{x} direction so that the microwave field b_{rms} produced by the transmission line is perpendicular to it. In this way, a quasi homogeneous Kittel magnon mode is excited in the ferromagnet (blue rectangle with colored arrows) lying at distance h from the superconductor. **c**: Enlarged view of the meander region (left panel) where finger capacitors are opened by FIB (right panel). **d**: The resulting CPW resonator, with characteristic frequency ω_p , and its coupling to the ferromagnetic sample are characterized using the VNA.

size that causes the Si_3N_4 palette to bend. We estimate $h \sim 4 \mu\text{m}$ for sample #2 and $h \sim 500 \text{ nm}$ for the rest. Samples #1 and #2 are located onto the as-fabricated transmission lines, sample #3 goes onto the $w = 1 \mu\text{m}$ wide constriction and, finally, sample #4 lies on top of the smallest $w = 240 \text{ nm}$ wide constriction (see Fig. 2a).

B. Broadband FMR

Samples are cooled down to 4.2 K in liquid helium in a cryostat containing a superconducting vector magnet. Broadband FMR experiments are performed by measuring the transmission coefficient S_{21} through the transmission line using a vector network analyzer (VNA) as schematized in Fig. 1b. The external magnetic field B_{ext} is used to polarize the ferromagnet parallel to the transmission line (\hat{x} direction) so that the microwave field produced by the superconductor (along the \hat{y} direction) can excite the homogeneous Kittel mode with frequency

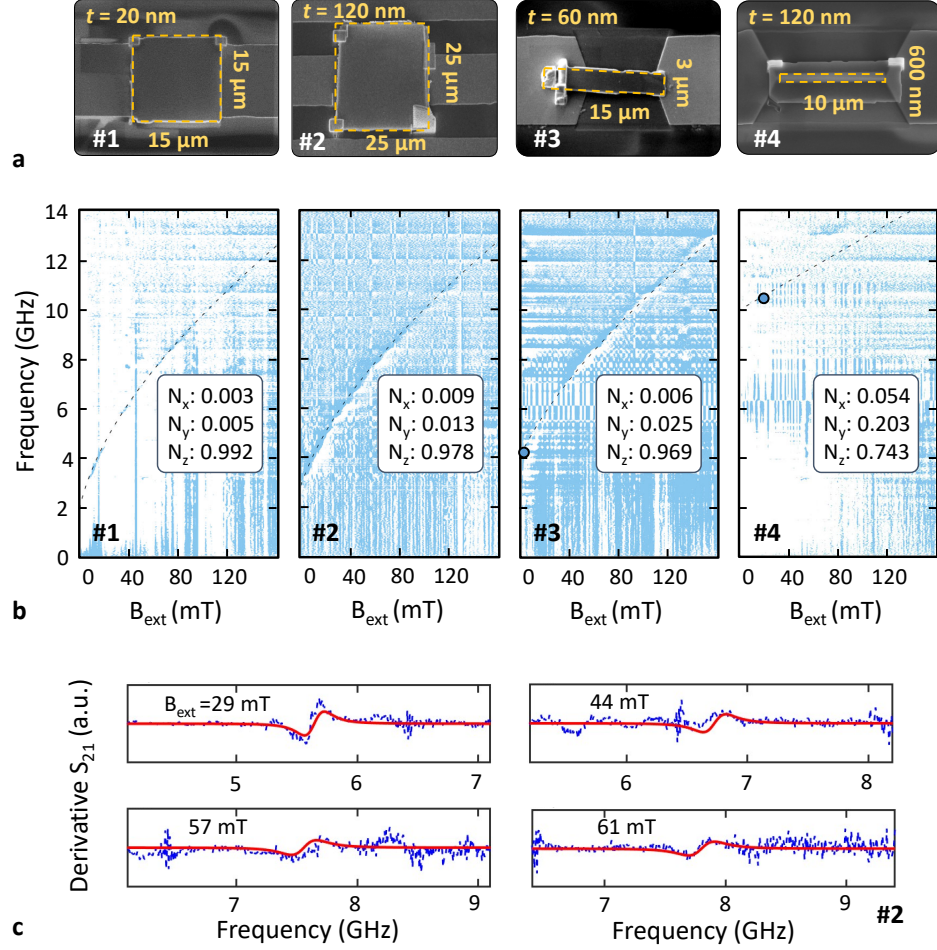


FIG. 2. **a**: SEM pictures of samples **#1**, **#2**, **#3** and **#4**, highlighted with yellow dashed polygons, placed onto the central line of CPW superconducting transmission lines. **b**: Broadband FMR curves of the same samples. Fitting the magnon resonance frequency ω_m to the general Kittel formula (Eq. 2, dashed) yields the corresponding demagnetizing factors (legend). The solid dots in panels **#3** and **#4** correspond to the experimental data points obtained from cavity experiments (see Fig. 3b). **c**: Field derivative of the experimental S_{21} parameter corresponding to sample **#2** (dashed blue) measured at different values of B_{ext} and fits based on Eq. 3 (solid red).

given by [19]:

$$\omega_m^2 = \gamma_e \left[B_{\text{ext}} + (N_y - N_x) \mu_0 M_s \right] \times \left[B_{\text{ext}} + (N_z - N_x) \mu_0 M_s \right]. \quad (2)$$

Here, $\mu_0 = 4\pi \times 10^{-7}$ Tm/A and $M_s = 0.86 \times 10^6$ A/m is the saturation magnetization of Py measured in a nominally identical substrate. Finally, N_x , N_y and N_z are the demagnetizing factors that satisfy $N_x + N_y + N_z = 1$. These factors can be determined analytically based on geometrical considerations [31].

Experimental curves corresponding to samples **#1**, **#2**, **#3** and **#4** are shown in Fig. 2b. The Kittel resonance frequency depends strongly on the aspect ratio of the Py sample. As a matter of fact, ω_m increases from 2 GHz up to more than 10 GHz at $B_{\text{ext}} \sim 0$ mT. Fitting the experimental curves with Eq. 2 allows extracting the demagnetizing factors (see insets of Fig. 2b). N_x increases

slightly with sample thickness but, in general, remains $\ll 1$ since \hat{x} is an easy magnetization axis. In case of samples **#1** and **#2**, symmetry considerations would yield $N_x = N_y$. However, this is not the case due to unavoidable imperfections that are especially dramatic in case of sample **#2** due to the above mentioned bending. In case of samples **#3** and **#4**, N_y increases considerably, indicating that the \hat{y} direction becomes progressively harder as the aspect ratio of the sample increases.

FMR data allow us to estimate the frequency-dependent magnon-photon coupling. From input-output theory, we can express the transmission through an open line as [32]:

$$T = 1 - \frac{\Gamma}{\Gamma + \gamma + i(\omega_m - \omega)}. \quad (3)$$

We recall that ω_m depends on the magnetic field through Eq. 2. In the above formula, $\gamma = 2\alpha\omega_m$ is the linewidth

	$\omega_p/2\pi$ (GHz)	$g_{\text{FMR}}/2\pi$ (MHz)	$g_{\text{res}}/2\pi$ (MHz)	$g_{\text{theo}}/2\pi$ (MHz)
#1	2.8	7	-	6.6
#2	3.5	16	-	17.3
#3	4.2	36	36	45.0
#4	10.5	66	72	72.4

TABLE I. Photon resonance frequency (ω_p); photon-magnon coupling determined from FMR measurements (g_{FMR}), from cavity experiments (g_{res}) and from theory (g_{theo}). The latter is calculated for $h = 4 \mu\text{m}$ in case of sample #2 and $h = 500 \text{ nm}$ for the rest.

of the ferromagnetic resonance and $\Gamma = g^2\pi/\omega_m$.

We calculate the field derivative of the absolute value of Eq. 3 and use the resulting equation to fit the derivative of the experimental data, i.e., $S_{21}(B_{\text{ext}}^{i+1}) - S_{21}(B_{\text{ext}}^i)$, where super-indexes i and $i+1$ refer to successive field values. A few representative curves corresponding to sample #2 are shown in Fig. 2c. From these fits we estimate $\alpha \sim 0.01$, i.e., the Py damping factor at cryogenic temperatures. This value is close to the Gilbert damping parameter measured at low and room temperatures [33]. On the other hand, we can estimate the frequency-dependent coupling g_{FMR} where the sub-index is used to indicate that these values are obtained from FMR experiments. Table I gives coupling values determined at some fixed frequencies $\omega_m = \omega_p$.

C. Cavity experiments

We next transform each transmission line into a resonator by opening gap capacitors using FIB milling (see Fig. 1c). In doing so, we chose the resulting cavity length to fit the $\lambda/2$ mode of the desired frequency ω_p summarized in Table I. Samples are again immersed in liquid helium except for sample #4 that is cooled down to 10 mK using a dilution refrigerator. The VNA is used to probe the S_{21} factor as a function of frequency while sweeping B_{ext} as described in the transmission line experiments (see Fig. 1d). Measurements performed on #1 and #2 suggest that these samples are in the weak magnon-photon coupling regime. On the other hand, two avoided crossings are clearly visible in the experimental data obtained with samples #3 and #4 (see Fig. 3a). These anticrossings appear at positive and negative magnetic fields, at the intersect with the FMR curves (dashed lines), which is a proof of strong coupling.

Cavity experiments can be also used to give an alternative estimate of the magnon-photon coupling. For this purpose we analyze the cavity resonance linewidth κ as a function of external magnetic field. The linewidth is evaluated by fitting the experimental S_{21} to a Fano-like resonance. The latter accounts better for asymmetries in our experimental data that likely arise from interference between the resonator and a small continuous background

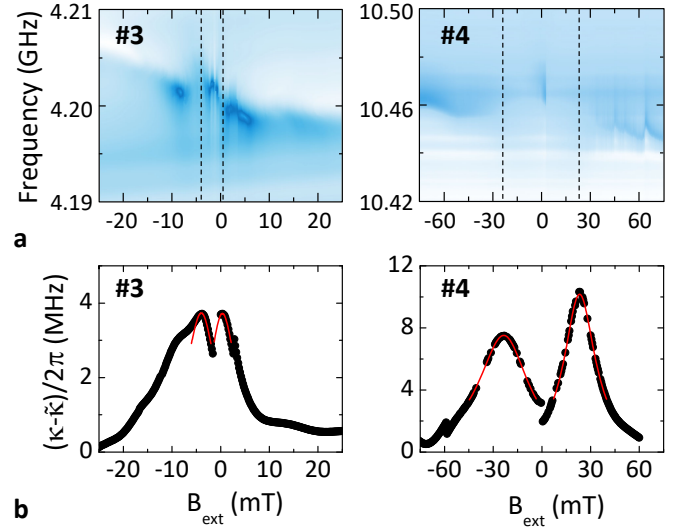


FIG. 3. **a**: Experimental microwave transmission through superconducting resonators containing samples #3 ($\omega_p/2\pi = 4.2 \text{ GHz}$, $T = 4.2 \text{ K}$) and #4 ($\omega_p/2\pi = 10.5 \text{ GHz}$, $T = 10 \text{ mK}$). The dashed lines are the broadband FMR curves shown in Fig. 2b. **b**: Field dependence of the resonance width κ for the same resonators and least-squares fits (dashed lines) to Eq. 4. Data corresponding to sample #3 are shifted 2 mT towards negative fields due to a small remnant field in the superconducting coils. Maxima of κ vs. B_{ext} provide two additional experimental points of FMR at $B_{\text{ext}} = -3.9$ and 0.4 mT for sample #3 and $B_{\text{ext}} = \pm 23 \text{ mT}$ for sample #4 (see Fig. 2b).

signal [34]. Depending on the coupling strength, the resonance broadens around the intersection field according to [35]:

$$\kappa = \tilde{\kappa} + \frac{\gamma g^2}{(\omega_p - \omega_m)^2 + \gamma^2}, \quad (4)$$

where $\tilde{\kappa}$ is the linewidth of the bare cavity that can be measured far from resonance. Again, we recall that ω_m depends on the external field through Eq. 2. Experimental κ vs. B_{ext} curves exhibit two clear maxima at positive and negative fields, where level repulsion occurs (Fig. 3b). Fitting these data to Eq. 4 gives a complementary estimate of the coupling (labelled g_{res}) that we summarize in Table I.

D. Theoretical model

We finish by comparing our experimental results with numerical estimations of the coupling factors. A generalization of formulas given in Refs. 36 and 37, where the field was considered homogeneous in the relevant region, is as follows. Each ferromagnetic sample is discretized into cells. The Hamiltonian interaction is given by $H_I = v_{\text{cell}} \sum_j \mathbf{m}_j \cdot \mathbf{b}_{\text{rms}}(\mathbf{r}_j)$. Here, v_{cell} and \mathbf{m}_j are the volume and magnetization of the cell, respectively, while $\mathbf{b}_{\text{rms}}(\mathbf{r}_j)$ is the vacuum field at the cell's position

\mathbf{r}_j . In each cell, the number of spins is large enough to perform the Holstein-Primakoff transformation, so the quantization of the magnetization can be written in terms of bosonic operators as $\mathbf{m}_j = \Delta\mathbf{M}_j(a_j^\dagger + a_j)$ where $\Delta\mathbf{M}_j$ is the position-dependent amplitude of the magnetization modulation. Once this is done, we define the *collective* mode [38]:

$$a = \frac{1}{\sqrt{\sum_j (\Delta\mathbf{M}_j \cdot \mathbf{b}_{\text{rms}}(\mathbf{r}_j))^2}} \sum_j \Delta\mathbf{M}_j \cdot \mathbf{b}_{\text{rms}}(\mathbf{r}_j) a_j$$

Finally, taking the continuum limit, the magnon-resonator coupling reads:

$$g^2 = \frac{\gamma}{4\hbar} \int_{V_m} (\mathbf{b}_{\text{rms}} \cdot \Delta\mathbf{M}) dV, \quad (5)$$

with V_m the volume of the ferromagnet. Equation 5 is valid for *any* kind of magnonic mode excited in the ferromagnet, including the Kittel mode studied here.

We first calculate \mathbf{b}_{rms} for the different resonators used in this work. To this end, we use the following expression for the zero-point current fluctuations [39]:

$$i_{\text{rms}} = \omega_p \sqrt{\frac{\hbar\pi}{4Z_0}}, \quad (6)$$

with $Z_0 = 50 \, \Omega$ the impedance of the circuit. Inserting the experimental frequencies ω_p into Eq. 6, we calculate i_{rms} for each resonator. From these values, we obtain the spatial distribution of \mathbf{b}_{rms} created by the superconducting cavity using the finite-element software 3D-MLSI that solves London equations in a user-defined superconducting circuit [40]. Figure 4a shows the resulting in-plane (y) component of \mathbf{b}_{rms} for the different samples calculated at the position of the ferromagnet. We highlight that b_{rms} increases by a factor ~ 30 from sample #1 to #4 stemming from the smallness of the patterned constriction.

On the other hand, we need to estimate $\Delta\mathbf{M}$ which depends on the spatial distribution of the excitation field, i.e., b_{rms} , and also on the non-homogeneous magnetic susceptibility of the ferromagnet. We use the micromagnetic solver MUMAX³ that allows calculating the time evolution of the magnetization resulting from a spatial-dependent excitation magnetic field in a user-defined ferromagnet [41]. Figure 4b shows the resulting y component of $\Delta\mathbf{M}$ for the different samples. Notice that this quantity depends strongly on the aspect ratio of each ferromagnet. The magnetic susceptibility of sample #1 is indeed substantially more homogeneous than that of the others. This is due to its small thickness that constrains the modulation of the magnetization to the plane.

Finally, we use Eq. 5 to calculate the theoretical coupling factors g_{theo} at fixed frequency ω_p for varying distance between the ferromagnet and the superconducting line, i.e., distance h in Fig. 1b and d. Results are plotted in Fig. 4c (solid lines) together with the experimental g values obtained at the same frequencies (scatter). The blue shaded area indicates the weak coupling region whereas strong magnon-photon coupling is expected for samples above the dashed blue line.

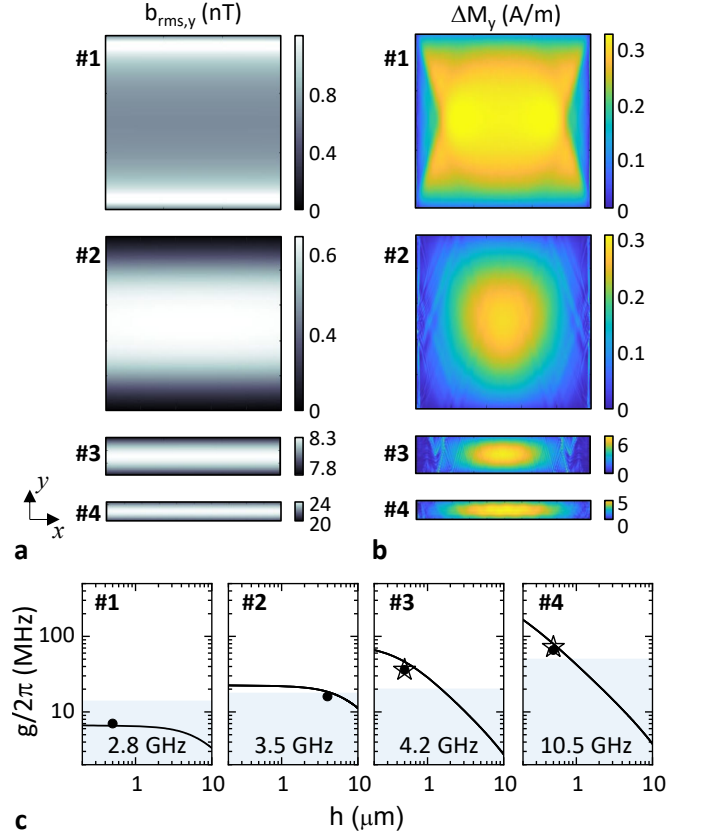


FIG. 4. Spatial distribution of the in-plane (y) component of \mathbf{b}_{rms} (a) and $\Delta\mathbf{M}$ (b) calculated at the position of the ferromagnet. c: Solid lines are the numerical g_{theo} (at fixed frequency ω_p given above each panel) vs. distance h . Data points are the experimental g_{FMR} (dots) and g_{res} (stars). Strong coupling is reached for g above the blue shaded region corresponding to $\gamma/4$. From left to right, our experimental data roughly follow $g \propto \omega_p$.

III. DISCUSSION

We first focus our attention on the experimental g_{FMR} and g_{res} and compare them to the g_{theo} calculated with the above theory (Table I). It is worth mentioning that, in case of samples #3 and #4, $g_{\text{FMR}} \approx g_{\text{res}}$, supporting the two experimental approaches followed here. On the other hand, the main source of error in the calculation of g_{theo} is the distance h . As shown in Fig. 4c, experiment and theory agree to a very good extent for the estimated values of h , confirming the validity of our model. Therefore, Eq. 5 can be used for calculating the coupling between superconducting circuits of whatever geometry and magnetostatic modes of any kind excited in ferromagnetic samples of arbitrary shape.

The strong coupling regime is achieved when $g > \kappa/4$ and $g > \gamma/4$. The latter condition is more demanding as our resonators have typical quality factors $Q = \omega_p/\kappa \sim 1 - 2 \times 10^3$ whereas the quality factor of Py amounts to just $\omega_m/\gamma = 1/2\alpha \sim 50$. As shown in Fig. 4c, samples

#1 and **#2** do not satisfy $g > \gamma/4$ being, therefore, in the weak coupling regime, as also evidenced by our cavity experiments. On the other hand, thanks to the small mode volume of the resonators containing samples **#3** and **#4**, they do satisfy the strong coupling condition, yielding the observation of level repulsion that is shown in Fig. 3a.

We can calculate the effective coupling per spin for samples **#3** and **#4** that amounts to 70 and 280 Hz, respectively. The latter is one order of magnitude larger than magnon-photon coupling values reported in the literature for thin-film Py samples coupled to distributed resonators [22, 23] and exceeds the largest spin-photon coupling strength measured with paramagnetic spins under similar conditions [26]. As a matter of fact, the g values reported here are similar to those obtained using optimized *LC*-resonators [22, 29]. Combining both approaches, i.e., patterning of nanoconstrictions with low-impedance resonators, shall increase the total coupling by 1 – 2 orders of magnitude.

Finally, our experimental data serve to demonstrate the direct relation between the coupling strength and the cavity frequency (see Fig. 4c). Deviations from the expected linear dependence arise from the different geometries of the resonators and the particular volumes and demagnetizing factors of each sample. The latter affects the magnetic susceptibility of the corresponding magnetostatic (Kittel) mode. Besides these factors, our experimental data roughly follow $g \propto \omega_p$. This is particularly evident for samples **#3** and **#4** exhibiting very similar filling factors. Increasing the cavity operation frequency from $\omega_p/2\pi = 4.2$ GHz (**#3**) up to $\omega_p/2\pi = 10.5$ GHz (**#4**) yields twice the coupling strength.

We stress that patterning nanoconstrictions or reducing the impedance yields a square-root increase of g while keeping the losses in the ferromagnet unchanged, meaning these approaches serve to increase the cooperativity. On the other hand, increasing the operation frequency yields a linear increase of g , at the cost of also increasing $\gamma = 2\alpha\omega_p$. That is to say, increasing ω_p does not ease entering into the strong coupling regime but does have the effect of linearly increasing the rate of information exchange between photon and magnon excitations.

IV. CONCLUSIONS

We demonstrate the possibility of tuning the operation frequency in cavity magnonics by controlling the shape of the ferromagnet. Varying the aspect ratio of different Py samples we reach operation frequencies up to 10.5 GHz at ~ 20 mT. Working at such high frequencies with isotropic spherical ferromagnets would have required an external field close to 0.4 T. High frequency operation together with the use of patterned nanoconstrictions in superconducting transmission lines enhances the net coupling between magnetic materials and cavity photons allowing us to reach an average single spin coupling of 280 Hz.

Our broadband FRM measurements and cavity experiments demonstrate that the magnon-photon coupling strength can be estimated using either open transmission lines or resonant cavities, yielding very good agreement. Additionally, we provide a simple recipe to theoretically calculate g in hybrid systems combining superconducting circuits and ferromagnetic materials. Our approach can be used to design quantum magnonic experiments exploiting not only the homogeneous Kittel mode but any higher order magnonic mode in ferromagnets of arbitrary size and shape and to tune the operation conditions, frequency and magnetic field, to fit those required in a particular experiment or application.

V. ACKNOWLEDGMENTS

This work was partly funded and supported by the spanish MCIN/ AEI /10.13039/501100011033/ and FEDER (*Una manera de hacer Europa*) through grant RTI2018-096075-B-C21, the BBVA Foundation through "Beca Leonardo a Investigadores y Creadores Culturales 2019", the Aragón Regional Government through project E09_20R (*Construyendo Europa desde Aragón*) and the EU through FET-OPEN (862893 FATMOLS) and the European Research Council (ERC) under the European Union's Horizon 2020 research and innovation programme (948986 QFaST). S. M.-L. R. acknowledges a FPI grant from the spanish MCIN. Authors would like to acknowledge the use of Servicio General de Apoyo a la Investigación-SAI, Universidad de Zaragoza.

-
- [1] A. Blais, J. Gambetta, A. Wallraff, D. I. Schuster, S. M. Girvin, M. H. Devoret, and R. J. Schoelkopf, Quantum-information processing with circuit quantum electrodynamics, *Physical Review A* **75**, 032329 (2007).
 - [2] M. Harder, B. M. Yao, Y. S. Gui, and C.-M. Hu, Coherent and dissipative cavity magnonics, *Journal of Applied Physics* **129**, 201101 (2021).
 - [3] Y. Li, W. Zhang, V. Tyberkevych, W.-K. Kwok, A. Hoffmann, and V. Novosad, Hybrid magnonics: Physics, circuits, and applications for coherent information process-

- ing, *Journal of Applied Physics* **128**, 130902 (2020).
- [4] D. Lachance-Quirion, Y. Tabuchi, A. Gloppe, K. Usami, and Y. Nakamura, Hybrid quantum systems based on magnonics, *Applied Physics Express* **12**, 070101 (2019).
- [5] Y. Tabuchi, S. Ishino, T. Ishikawa, R. Yamazaki, K. Usami, and Y. Nakamura, Hybridizing ferromagnetic magnons and microwave photons in the quantum limit, *Physical Review Letters* **113**, 083603 (2014).
- [6] H. Huebl, C. W. Zollitsch, J. Lotze, F. Hocke, M. Greifenstein, A. Marx, R. Gross, and S. T. B. Goennenwein,

- High cooperativity in coupled microwave resonator ferromagnetic insulator hybrids, *Physical Review Letters* **111**, 127003 (2013).
- [7] I. A. Golovchanskiy, N. N. Abramov, V. S. Stolyarov, M. Weides, V. V. Ryazanov, A. A. Golubov, A. V. Ustinov, and M. Y. Kupriyanov, Ultrastrong photon-to-magnon coupling in multilayered heterostructures involving superconducting coherence via ferromagnetic layers, *Science Advances* **7**, 10.1126/sciadv.abe8638 (2021).
 - [8] X. Zhang, C.-L. Zou, L. Jiang, and H. X. Tang, Strongly coupled magnons and cavity microwave photons, *Physical Review Letters* **113**, 156401 (2014).
 - [9] N. J. Lambert, A. Rueda, F. Sedlmeir, and H. G. L. Schwefel, Coherent conversion between microwave and optical photons—an overview of physical implementations, *Advanced Quantum Technologies* **3**, 1900077 (2020).
 - [10] R. Hisatomi, A. Osada, Y. Tabuchi, T. Ishikawa, A. Noguchi, R. Yamazaki, K. Usami, and Y. Nakamura, Bidirectional conversion between microwave and light via ferromagnetic magnons, *Physical Review B* **93**, 174427 (2016).
 - [11] Y. Li, V. G. Yefremenko, M. Lisovenko, C. Trevillian, T. Polakovic, T. W. Cecil, P. S. Barry, J. Pearson, R. Divan, V. Tyberkevych, C. L. Chang, U. Welp, W.-K. Kwok, and V. Novosad, Coherent coupling of two remote magnonic resonators mediated by superconducting circuits, *Physical Review Letters* **128**, 047701 (2022).
 - [12] D. Lachance-Quirion, S. P. Wolski, Y. Tabuchi, S. Kono, K. Usami, and Y. Nakamura, Entanglement-based single-shot detection of a single magnon with a superconducting qubit, *Science* **367**, 425 (2020).
 - [13] S. Wolski, D. Lachance-Quirion, Y. Tabuchi, S. Kono, A. Noguchi, K. Usami, and Y. Nakamura, Dissipation-based quantum sensing of magnons with a superconducting qubit, *Physical Review Letters* **125**, 117701 (2020).
 - [14] Y.-Y. Wang, S. van Geldern, T. Connolly, Y.-X. Wang, A. Shilcuskys, A. McDonald, A. A. Clerk, and C. Wang, Low-loss ferrite circulator as a tunable chiral quantum system, *Physical Review Applied* **16**, 064066 (2021).
 - [15] N. Zhu, X. Han, C.-L. Zou, M. Xu, and H. X. Tang, Magnon-photon strong coupling for tunable microwave circulators, *Physical Review A* **101**, 043842 (2020).
 - [16] X. Zhang, A. Galda, X. Han, D. Jin, and V. M. Vinokur, Broadband nonreciprocity enabled by strong coupling of magnons and microwave photons, *Physical Review Applied* **13**, 044039 (2020).
 - [17] Y.-P. Wang, J. Rao, Y. Yang, P.-C. Xu, Y. Gui, B. Yao, J. You, and C.-M. Hu, Nonreciprocity and unidirectional invisibility in cavity magnonics, *Physical Review Letters* **123**, 127202 (2019).
 - [18] D. M. Pozar, *Microwave engineering* (Wiley, 2011).
 - [19] C. Kittel and D. F. Holcomb, Introduction to solid state physics, *American Journal of Physics* **35**, 547 (1967).
 - [20] L. R. Walker, Magnetostatic modes in ferromagnetic resonance, *Physical Review* **105**, 390 (1957).
 - [21] L. Mihalceanu, V. I. Vasyuchka, D. A. Bozhko, T. Langner, A. Y. Nechiporuk, V. F. Romanyuk, B. Hillebrands, and A. A. Serga, Temperature-dependent relaxation of dipole-exchange magnons in yttrium iron garnet films, *Physical Review B* **97**, 214405 (2018).
 - [22] J. T. Hou and L. Liu, Strong coupling between microwave photons and nanomagnet magnons, *Physical Review Letters* **123**, 107702 (2019).
 - [23] Y. Li, T. Polakovic, Y.-L. Wang, J. Xu, S. Lendinez, Z. Zhang, J. Ding, T. Khaire, H. Saglam, R. Divan, J. Pearson, W.-K. Kwok, Z. Xiao, V. Novosad, A. Hoffmann, and W. Zhang, Strong coupling between magnons and microwave photons in on-chip ferromagnet-superconductor thin-film devices, *Physical Review Letters* **123**, 107701 (2019).
 - [24] I. Haygood, M. Pufall, E. Edwards, J. M. Shaw, and W. Rippard, Strong coupling of an fe-co alloy with ultralow damping to superconducting co-planar waveguide resonators, *Physical Review Applied* **15**, 054021 (2021).
 - [25] M. A. W. Schoen, D. Thonig, M. L. Schneider, T. J. Silva, H. T. Nembach, O. Eriksson, O. Karis, and J. M. Shaw, Ultra-low magnetic damping of a metallic ferromagnet, *Nature Physics* **12**, 839 (2016).
 - [26] I. Gimeno, W. Kersten, M. C. Pallarés, P. Hermosilla, M. J. Martínez-Pérez, M. D. Jenkins, A. Angerer, C. Sánchez-Azqueta, D. Zueco, J. Majer, A. Lostao, and F. Luis, Enhanced molecular spin-photon coupling at superconducting nanoconstrictions, *ACS Nano* **14**, 8707 (2020).
 - [27] P. Haikka, Y. Kubo, A. Bienfait, P. Bertet, and K. Mølmer, Proposal for detecting a single electron spin in a microwave resonator, *Physical Review A* **95**, 022306 (2017).
 - [28] M. D. Jenkins, U. Naether, M. Ciria, J. Sesé, J. Atkinson, C. Sánchez-Azqueta, E. del Barco, J. Majer, D. Zueco, and F. Luis, Nanoscale constrictions in superconducting coplanar waveguide resonators, *Applied Physics Letters* **105**, 162601 (2014).
 - [29] S. Probst, A. Bienfait, P. Campagne-Ibarcq, J. J. Pla, B. Albanese, J. F. D. S. Barbosa, T. Schenkel, D. Vion, D. Esteve, K. Mølmer, J. J. L. Morton, R. Heeres, and P. Bertet, Inductive-detection electron-spin resonance spectroscopy with 65 spins/hz sensitivity, *Applied Physics Letters* **111**, 202604 (2017).
 - [30] C. Eichler, A. Sigillito, S. Lyon, and J. Petta, Electron spin resonance at the level of 10^4 spins using low impedance superconducting resonators, *Physical Review Letters* **118**, 037701 (2017).
 - [31] A. Aharoni, Demagnetizing factors for rectangular ferromagnetic prisms, *Journal of Applied Physics* **83**, 3432 (1998).
 - [32] D. Roy, C. Wilson, and O. Firstenberg, Colloquium: Strongly interacting photons in one-dimensional continuum, *Reviews of Modern Physics* **89**, 021001 (2017).
 - [33] Y. Zhao, Q. Song, S.-H. Yang, T. Su, W. Yuan, S. S. P. Parkin, J. Shi, and W. Han, Experimental investigation of temperature-dependent gilbert damping in permalloy thin films, *Scientific Reports* **6**, 10.1038/srep22890 (2016).
 - [34] U. Fano, Effects of configuration interaction on intensities and phase shifts, *Physical Review* **124**, 1866 (1961).
 - [35] P. Bushev, A. K. Feofanov, H. Rotzinger, I. Protopopov, J. H. Cole, C. M. Wilson, G. Fischer, A. Lukashenko, and A. V. Ustinov, Ultralow-power spectroscopy of a rare-earth spin ensemble using a superconducting resonator, *Physical Review B* **84**, 060501 (2011).
 - [36] M. J. Martínez-Pérez and D. Zueco, Quantum electrodynamics with magnetic textures, *New Journal of Physics* **21**, 115002 (2019).
 - [37] M. J. Martínez-Pérez and D. Zueco, Strong coupling of a single photon to a magnetic vortex, *ACS Photonics* **6**, 360 (2018).

- [38] T. Hümmer, G. M. Reuther, P. Hänggi, and D. Zueco, Nonequilibrium phases in hybrid arrays with flux qubits and nitrogen-vacancy centers, *Phys. Rev. A* **85**, 052320 (2012).
- [39] M. Jenkins, T. Hümmer, M. J. Martínez-Pérez, J. García-Ripoll, D. Zueco, and F. Luis, Coupling single-molecule magnets to quantum circuits, *New Journal of Physics* **15**, 095007 (2013).
- [40] M. M. Khapaev, M. Y. Kupriyanov, E. Goldobin, and M. Siegel, Current distribution simulation for superconducting multi-layered structures, *Superconductor Science and Technology* **16**, 24 (2002).
- [41] A. Vansteenkiste, J. Leliaert, M. Dvornik, M. Helsen, F. Garcia-Sanchez, and B. V. Waeyenberge, The design and verification of MuMax3, *AIP Advances* **4**, 107133 (2014).